

2D Empirical Transforms. Wavelets, Ridgelets and Curvelets revisited

Jérôme Gilles and Giang Tran and Stanley Osher *

November 1, 2024

Abstract

A recently developed new approach, called “Empirical Wavelet Transform”, aims to build 1D adaptive wavelet frames accordingly to the analyzed signal. In this paper, we present several extensions of this approach to 2D signals (images). We revisit some well-known transforms (tensor wavelets, Littlewood-Paley wavelets, ridgelets and curvelets) and show that it is possible to build their empirical counterpart. We prove that such constructions lead to different adaptive frames which show some promising properties for image analysis and processing.

1 Introduction

Wavelets and their geometric extensions (framelets, ridgelets, curvelets, . . .) are not only a useful mathematical tool arising in harmonic analysis and used to study function spaces, but they are also very efficient in image processing. For instance, in texture analysis, such transforms permit us to extract relevant characteristics which can be used as inputs of a classifier. Since the advent of compressive sensing theory, many variational models have been proposed in the literature, using the sparsity properties in these transform domains [4, 5, 6, 27, 29], to perform efficient denoising or deconvolution. While wavelets are well established in the scientific community, their foundation has not really evolved since their origin and almost all discrete wavelet bases are built on a prescribed scheme corresponding to the multiresolution analysis definition. The main consequence of using such a definition is that those basis are based on dyadic scale decomposition which does not ensure that the corresponding filters are the optimal ones to represent an image. For instance, it is easy to build a texture based on compact information lying between two scales and which will be separated by a usual wavelet transform. A better approach is to have an adaptive representation where the basis is generated accordingly to the information contained in the image itself. Surprisingly, there are only a few attempts to build such adaptive representations. One of the first ones was the Brushlet transform [3, 23] which aims to build some wavelet filters based on adaptive supports in the Fourier domain. While this construction is difficult to implement and

*University of California, Los Angeles (UCLA), Department of Mathematics, 520 Portola Plaza, Los Angeles, CA 90095 (jgilles@math.ucla.edu, giangtran@math.ucla.edu, sjo@math.ucla.edu)

did not get a real success, the corresponding idea is interesting and, as we will present later, will inspire our work. Mallat and his students investigated the opportunity to extract some geometric information from the image itself to build adaptive wavelets representations like the bandlet transform [20, 21, 25] or the geometrical grouplet transform [22]. A completely different approach to design an adaptive representation exists in the literature: the empirical mode decomposition (EMD). In the 1D case, the EMD was proposed by Huang et al. [19] where the aim of the method is to extract amplitude modulated-frequency modulated (AM-FM) components of an input signal. In practice, it is based on the detection of the upper and lower envelopes which provide the global trend of the signal. This low varying signal is then subtracted to the original one to get the highest oscillatory component. This procedure is repeated until all oscillating parts are extracted. Bidimensional extensions [12, 24] of this algorithm were proposed to process images. The main drawback of the EMD approach is that it is a pure nonlinear algorithmic procedure and the obtained representation is implementation dependent (e.g it depends on how the envelopes are detected, which interpolation process is used and the chosen stopping criteria). Moreover due to the nonlinear aspects, no theoretical background supports this method. Recently, in [17] the author proposed the construction of 1D empirical wavelets where the aim is, like the EMD, to extract AM-FM components from a signal. The definition of the empirical wavelets is based on the formulation of a Littlewood-Paley [18] wavelet where the choice of their supports in the Fourier domain is not prescribed to a dyadic tiling but chosen accordingly to the analyzed signal. The author showed that it is possible to build a wavelet tight frame which corresponds to an adaptive filter bank. The empirical wavelet transform (EWT) consists of two major steps: detect the Fourier supports and build the corresponding wavelet accordingly to those supports; filter the input signal with the obtained filter bank to get the different components. In [17], a straightforward tensor extension was proposed to do some image analysis. In this paper, we propose to investigate the possibility of generalizing this empirical approach to different existing 2D wavelet transforms. The remainder of the paper is as follows. In section 2, we define some notations which will be used throughout the paper and we recall the definition of the 1D EWT. In section 3, we investigate an important aspect of the EWT: the detection of the Fourier supports. Section 4 recalls the 2D tensor extension while sections 5, 6 and 7 present the empirical extensions of the 2D Littlewood-Paley wavelet transform, the ridgelet transform and the curvelet transform, respectively. Some experiments will be given in section 9 and we conclude in section 10.

2 Background

2.1 Notation

Let us start to fix some notations which will be used throughout the paper. We denote $\mathbf{x} = (x_1, x_2)$ a spatial position in the 2D plane, $\phi = (\omega_1, \omega_2)$ the coordinates in the 2D frequency plane (in the case of a 1D signal we will use ω to represent the 1D frequency). The convolution product will be denoted by \star . We define the following operators:

- $\mathcal{F}_{1,y}, \mathcal{F}_{1,y}^*$ the usual 1D Fourier transform and its inverse with respect to

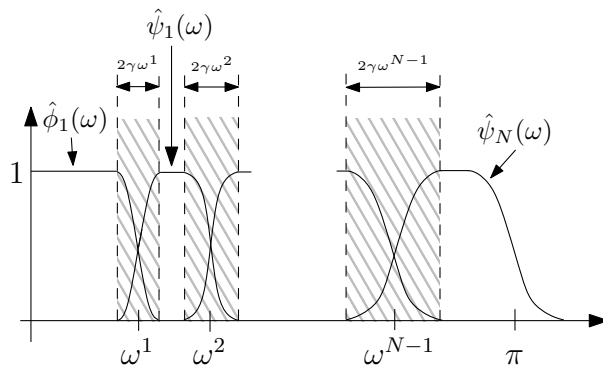


Figure 1: Fourier line decomposition principle and EWT basis construction.

the y variable,

- $\mathcal{F}_2, \mathcal{F}_2^*$ the usual 2D Fourier transform and its inverse,
- $\mathcal{F}_P, \mathcal{F}_P^*$ the 2D Pseudo-Polar Fourier transform and its adjoint [1] (their definitions are recalled in appendix A),
- $\mathcal{W}_{1,y}, \mathcal{W}_{1,y}^*$ the standard dyadic 1D wavelet transform and its inverse with respect to the y variable,

2.2 The 1D EWT

In [17], the author proposed to build an empirical wavelet transform (EWT). The idea consists of defining a bank of N wavelet filters (one lowpass and $N - 1$ bandpass filters corresponding to the approximation and details components, respectively) based on “well chosen” Fourier supports (meaning we select relevant modes in the signal spectrum). If we denote $f(t)$ a 1D signal, then we first detect the boundaries of each Fourier support from $|\mathcal{F}_{1,t}(f)|(\omega)$ (we will give more details about the procedure to detect such supports in section 3). This operation provides us with a set of boundaries $\Omega = \{\omega^n\}_{n=0,\dots,N}$ (we restrict our discussion to the interval $[0, \pi]$ and take the convention $\omega^0 = 0$ and $\omega^N = \pi$). Based on Ω (see Figure. 1), we can define a wavelet tight frame, $\mathcal{B} = \{\phi_1(t), \{\psi_n(t)\}_{n=1}^{N-1}\}$, inspired from Meyer’s and Littlewood-Paley wavelets, their Fourier transforms are given by:

$$\mathcal{F}_{1,t}(\phi_1)(\omega) = \begin{cases} 1 & \text{if } |\omega| \leq (1 - \gamma)\omega^1 \\ \cos \left[\frac{\pi}{2}\beta \left(\frac{1}{2\gamma\omega^1} (|\omega| - (1 - \gamma)\omega^1) \right) \right] & \text{if } (1 - \gamma)\omega^1 \leq |\omega| \leq (1 + \gamma)\omega^1 \\ 0 & \text{otherwise,} \end{cases} \quad (1)$$

and

$$\mathcal{F}_{1,t}(\psi_n)(\omega) = \begin{cases} 1 & \text{if } (1 + \gamma)\omega^n \leq |\omega| \leq (1 - \gamma)\omega^{n+1} \\ \cos \left[\frac{\pi}{2} \beta \left(\frac{1}{2\gamma\omega^{n+1}} (|\omega| - (1 - \gamma)\omega^{n+1}) \right) \right] & \text{if } (1 - \gamma)\omega^{n+1} \leq |\omega| \leq (1 + \gamma)\omega^{n+1} \\ \sin \left[\frac{\pi}{2} \beta \left(\frac{1}{2\gamma\omega^n} (|\omega| - (1 - \gamma)\omega^n) \right) \right] & \text{if } (1 - \gamma)\omega^n \leq |\omega| \leq (1 + \gamma)\omega^n \\ 0 & \text{otherwise.} \end{cases} \quad (2)$$

Where β is an arbitrary $\mathcal{C}^k([0, 1])$ function, fulfilling the properties $\beta(x) = 0$ if $x \leq 0$, $\beta(x) = 1$ if $x \geq 1$ and $\beta(x) + \beta(1 - x) = 1, \forall x \in [0, 1]$. For instance, in the construction of Meyer's wavelet, Daubechies [13] proposed to use

$$\beta(x) = \begin{cases} 0 & \text{if } x \leq 0 \\ 1 & \text{if } x \geq 1 \\ x^4(35 - 84x + 70x^2 - 20x^3) & \text{if } \forall x \in [0, 1]. \end{cases} \quad (3)$$

The parameter γ allows us to ensure that two consecutive transitions areas (dashed regions in Figure. 1) do not overlap. A necessary condition on γ is given in [17] in order to have the tight frame property of \mathcal{B} and allows us to automatically choose this parameter. Equipped with this set of filters, the 1D empirical wavelet transform (1D-EWT) is defined by

$$\mathcal{W}^{\mathcal{E}}(f)(n, t) = \mathcal{F}_{1,\omega}^* \left(\mathcal{F}_{1,t}(f)(\omega) \overline{\mathcal{F}_{1,t}(\psi_n)(\omega)} \right), \quad (4)$$

for the detail coefficients and the approximation coefficients (we adopt the convention $\mathcal{W}_f^{\mathcal{E}}(0, t)$ to denote them) by:

$$\mathcal{W}^{\mathcal{E}}(f)(0, t) = \mathcal{F}_{1,\omega}^* \left(\mathcal{F}_{1,t}(f)(\omega) \overline{\mathcal{F}_{1,t}(\phi_1)(\omega)} \right). \quad (5)$$

The inverse transform is straightforward by using inverse/adjoint operators:

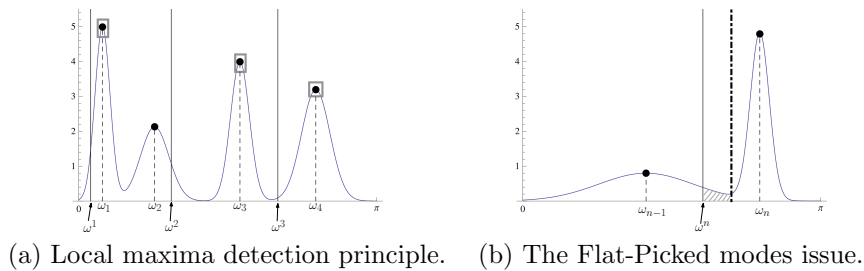
$$f(t) = \mathcal{W}^{\mathcal{E}}(f)(0, t) \star \phi_1(t) + \sum_{n=1}^{N-1} \mathcal{W}^{\mathcal{E}}(f)(n, t) \star \psi_n(t) \quad (6)$$

$$= \mathcal{F}_{1,\omega}^* \left(\mathcal{F}_{1,t}(\mathcal{W}^{\mathcal{E}})(0, \omega) \mathcal{F}_{1,t}(\phi_1)(\omega) + \sum_{n=1}^{N-1} \mathcal{F}_{1,t}(\mathcal{W}^{\mathcal{E}})(n, \omega) \mathcal{F}_{1,t}(\psi_n)(\omega) \right). \quad (7)$$

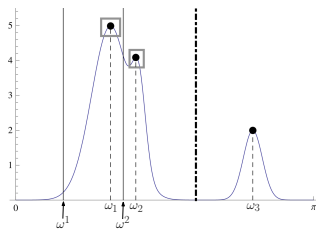
This EWT shows interesting results in extracting different information contained in the signal and permits us to obtain, with the help of the Hilbert transform, a precise time-frequency representation for 1D signals [17]. It is clear that the process detecting the Fourier boundaries is an important step. The next section recalls the approach used in [17] and proposes new ones.

3 Fourier boundaries detection

The original method proposed in [17] to detect the set of Fourier boundaries, Ω , is based on the detection of local maxima in the spectrum magnitude, assuming



(a) Local maxima detection principle. (b) The Flat-Picked modes issue.



(c) Global v.s local modes

Figure 2: Fourier supports definition based on local maxima detection and two of its main issues. See the text for full explanation.

that the spectrum is composed of sufficiently separated modes. However, in the case of images, except for highly textured images, their spectra do not exhibit obvious distinct modes and other criteria must be used to detect useful Fourier supports. After recalling the method based on the local maxima, we will introduce some improvements as well as other options to perform this detection task on the Fourier spectrum. In the following, we use the notation $H(\omega) = |\mathcal{F}_{1,y}|(\omega)$, restricted to $\omega \in [0, \pi]$ and we keep the convention given in section 2.2: $\omega^0 = 0$ and $\omega^N = \pi$.

3.1 Original detection of local maxima method

In this approach, see Figure. 2.a, we first compute all local maxima M_i of H (the black dots on the figure) and deduce their corresponding position ω_i . Next we keep the set of all ω_i corresponding to the $N - 1$ largest maxima (the square boxes on Figure. 2 illustrate the selected maxima when $N = 4$) and re-index them as ω_n where $1 \leq n \leq N - 1$. Finally we deduce the set of Fourier boundaries $\Omega = \{\omega^n\}_{n=0, \dots, N}$ (the solid vertical lines in the figure) by ($\omega_0 = 0$):

$$\omega^0 = 0 \quad ; \quad \omega^N = \pi; \quad \omega^n = \frac{\omega_n + \omega_{n-1}}{2} \quad \text{for } 1 \leq n \leq N - 1 \quad (8)$$

This simple method is efficient when the spectrum is composed of relatively well separated modes but can provide unexpected segmentation in some specific, but frequent in practice, cases. For instance, let us consider two close consecutive modes where one has a wide support while the other has a narrow support (see Figure. 2.b). It is straightforward to see that the corresponding boundary ω^n obtained from the above process will fall in the largest support of the first mode. This implies that the dashed area on the figure will be considered in the second

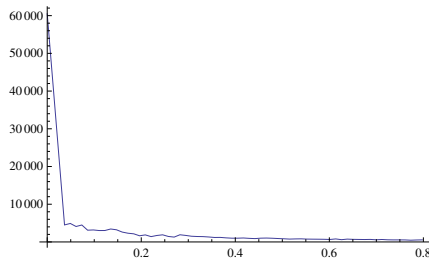


Figure 3: Example of a profile extracted from the spectrum of a natural image.

mode while it is obviously part of the first mode. In fact a “good” segmentation should correspond the dot-dashed vertical line instead of the solid vertical line. A second example where this method does not provide the best segmentation is when several local maxima belong to the same mode and are larger than other modes. Figure 2.c illustrates this case. Imagine we want three bands, the square boxes show the selected local maxima and the solid vertical lines represent the found Fourier boundaries. Conceptually, it will be more reasonable to consider that ω_1 and ω_2 are part of the same mode and then keep ω_3 instead of ω_2 (giving the dot-dashed vertical line as the second Fourier boundary and hence well separating to two modes). In this case, the problem comes from the fact that the segmentation method considers only a local information but it should be better to also take into account the spectrum global trend to avoid such issues.

3.1.1 Finding the lowest minima

The issue depicted on Figure 2.b is due to the fact that the boundary between two consecutive detected maxima is computed as the point at equal distance from the two maxima (Eq. 8). A simple way to avoid such situation is to retain the position of the lowest minima in the segment defined by consecutive maxima (this correspond to find the global minimum in this segment). If we denote \mathcal{U}_n the set of all local minima located between ω_{n-1} and ω_n , then

$$\omega^0 = 0 \quad ; \quad \omega^N = \pi; \quad \omega^n = \arg \min_{\omega} \mathcal{U}_n \quad \text{for } 1 \leq n \leq N - 1 \quad (9)$$

For instance, the use of this method will automatically provide the dot-dashed boundary of Figure. 2.b.

3.1.2 Global trend removing

The example showed on Figure. 2.c illustrates that many local maxima can belong to a common mode and may induce many unexpected boundaries. Such situation is quite common when we look at the spectrum profile of an image where the low frequencies concentrate a lot of the energy (see Figure. 3) with many local maxima but belonging to the same mode. In order to get rid of this situation, it should be interesting to work with the logarithm of H and/or to remove the global trend (denoted $T(\omega)$) of the analyzed spectrum before the detection task. Different approaches can be used to find the global trend of H . In this paper we propose different options:

- “*plaw*”: we approximate H with a power law of the form $T(\omega) = \omega^{-s}$. The exponent s can be estimated by using a least mean square criteria. In its discrete version it is equivalent to:

$$s = \arg \min \|H(\omega) - \omega^{-s}\|_2 = -\frac{\sum_n \ln \omega_n \ln H(\omega_n)}{\sum_n (\ln \omega_n)^2}. \quad (10)$$

- “*poly*”: we approximate H with a polynomial of degree d . Usual methods (mean square error) can be used to compute the polynomial coefficients. Concerning the polynomial degree, there is no automatic way to choose it and we will consider it as a parameter of this method. In practice, experiments seem to indicate that $d \approx 5$ works for usual images.
- “*morpho*”: this approach is inspired from the mathematical morphology [26, 28], see appendix B for a review of the mathematical morphology operators used in this paper. The opening operator (Op) provides a lower envelope of H while the closing operator (Cl) provides an upper envelope. Then the global trend can be obtained by

$$T(\omega) = \frac{Op(H, b)(\omega) + Cl(H, b)(\omega)}{2}. \quad (11)$$

Concerning the size of the structuring function b , because we want to remove the quickly changes in H , we can choose a size equal to the smallest distance between two consecutive maxima.

- “*tophat*”: this method, also based on mathematical morphology, consists to choose $T(\omega) = Op(H, b)(\omega)$. The size of b is chosen like in the *morpho* case.

3.2 Fine to Coarse histogram segmentation algorithm

In [14], the authors propose a fully automatic algorithm to detect the modes in an histogram. In our context, H can be viewed as an histogram representing how the energy is distributed among the frequencies. Then we can use this algorithm on H . The main advantage of this method is in that it automatically selects the number of modes. It is based on a fine to coarse segmentation of H . The algorithm is initialized with all local minima of H . The authors defined a statistical criteria to decide if two consecutive supports correspond to a common global trend or if they are part of true separated modes; this criteria is based on the ϵ -meaningful events theory [14, 15]. The (parameterless) algorithm can be resumed as following: start from the fine segmentation given by all local minima, choose one minimum and check if adjacent supports are part of a same trend or not. If yes then merge these supports by removing this local minima from the list. Repeat until no merging are possible.

3.3 Comparison of the different approaches

In order to understand the advantages and disadvantages of each method, we test each combination on two types of spectrum. The first one has a global trend with a huge magnitude difference between the low frequencies and the rest of the spectrum. The second one is mainly composed of distinct modes with a fast

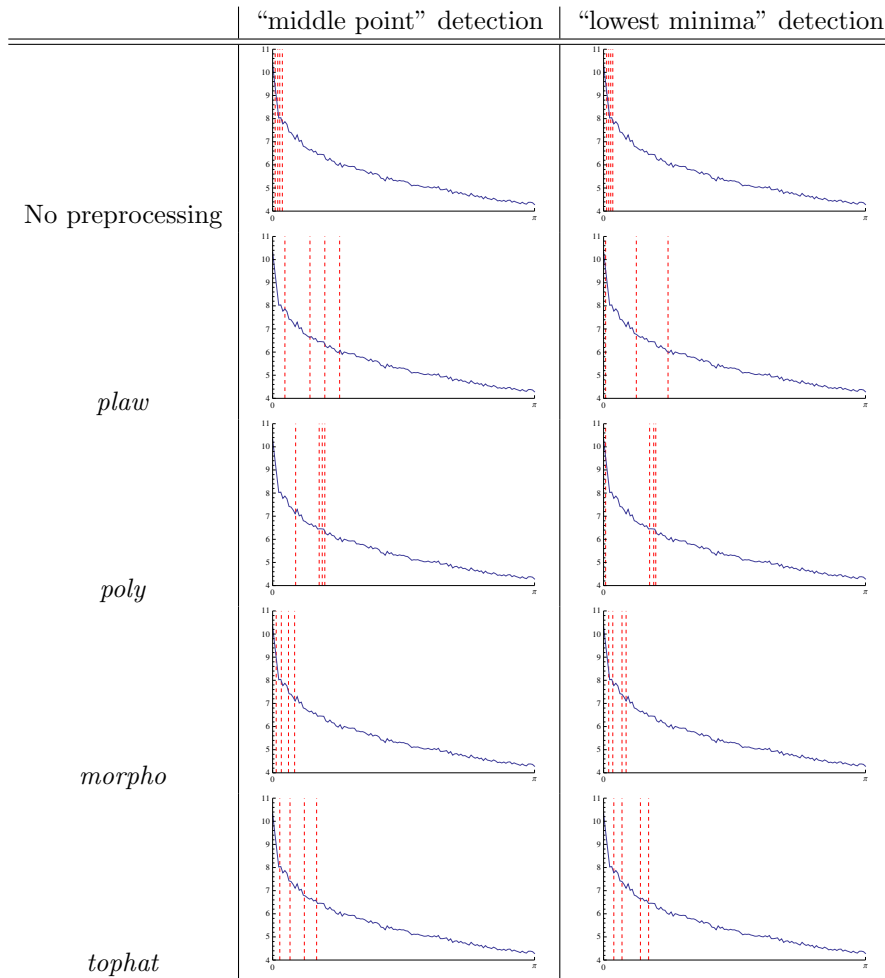


Figure 4: Fourier support detection on a spectrum with a global trend (without any logarithm and $N = 5$). Each row correspond to different preprocessing: none, *plaw*, *poly* and *morpho*, respectively. On the left column the detection based on the middle point between consecutive maxima is shown while the right column show the results when we keep the lowest minimum between consecutive maxima.

decaying global trend localized in the low frequencies. The respective detected Fourier boundaries are presented in Figures. 4, 5, 6 and 7, respectively. We can observe in the case of the spectrum with a global trend that it is necessary to do a preprocessing in order to magnify some “small” modes. Moreover, we see that by using the logarithm of the spectrum, all preprocessing methods provide interesting detections (notice that the boundary closest to π detected by the *morpho* method is not an artifact but a very small mode, too small to be visible on the provided graphs). In the case of the second spectrum with distinct modes, there are no specific advantages to take the logarithm. If the detection without any preprocessing gives interesting results, we can see that the use of the *plaw*

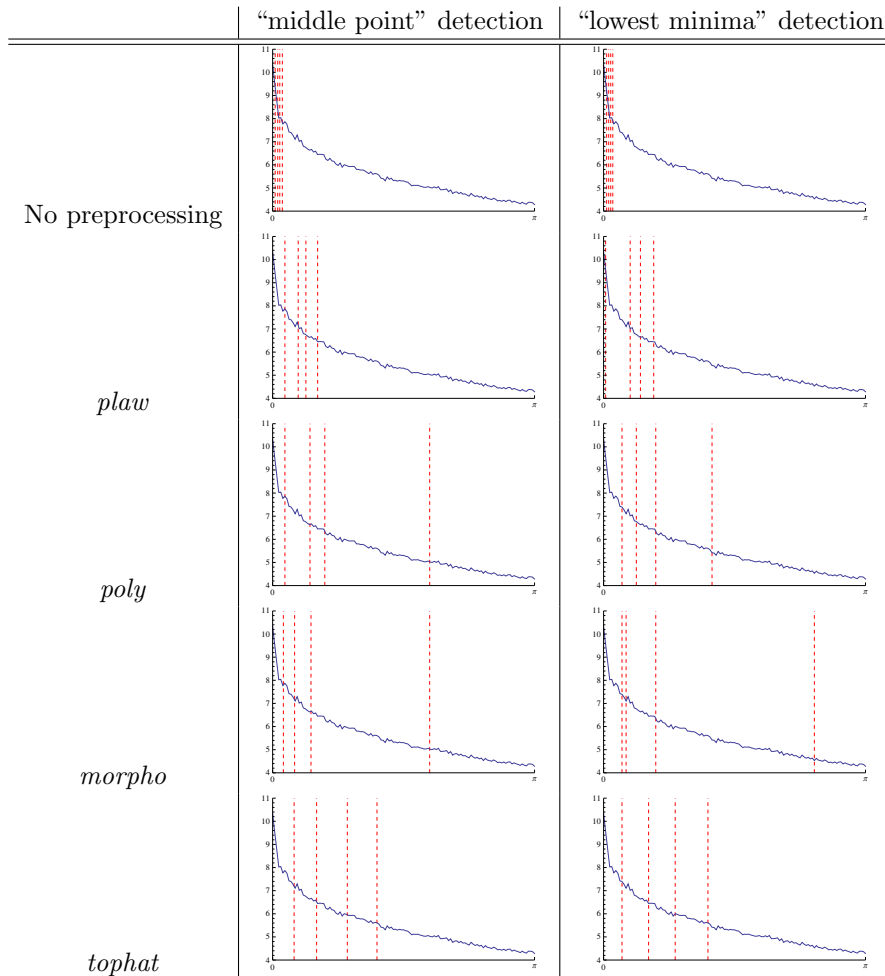


Figure 5: Fourier support detection on a spectrum with a global trend (with applying the logarithm and $N = 5$). Each row correspond to different preprocessing: none, *plaw*, *poly* and *morpho*, respectively. On the left column the detection based on the middle point between consecutive maxima is shown while the right column show the results when we keep the lowest minimum between consecutive maxima.

method permits to deal with the fast decaying trend. The results of the Fine to Coarse algorithm are given in Figure. 8. If this algorithm performs well in the case of distinct modes, it looks like it over segments the spectrum with the global trend.

4 Tensor 2D EWT

In [17], the author proposed to extend the 1D EWT to images by considering a tensor product approach as with the usual 2D discrete wavelet transform. The

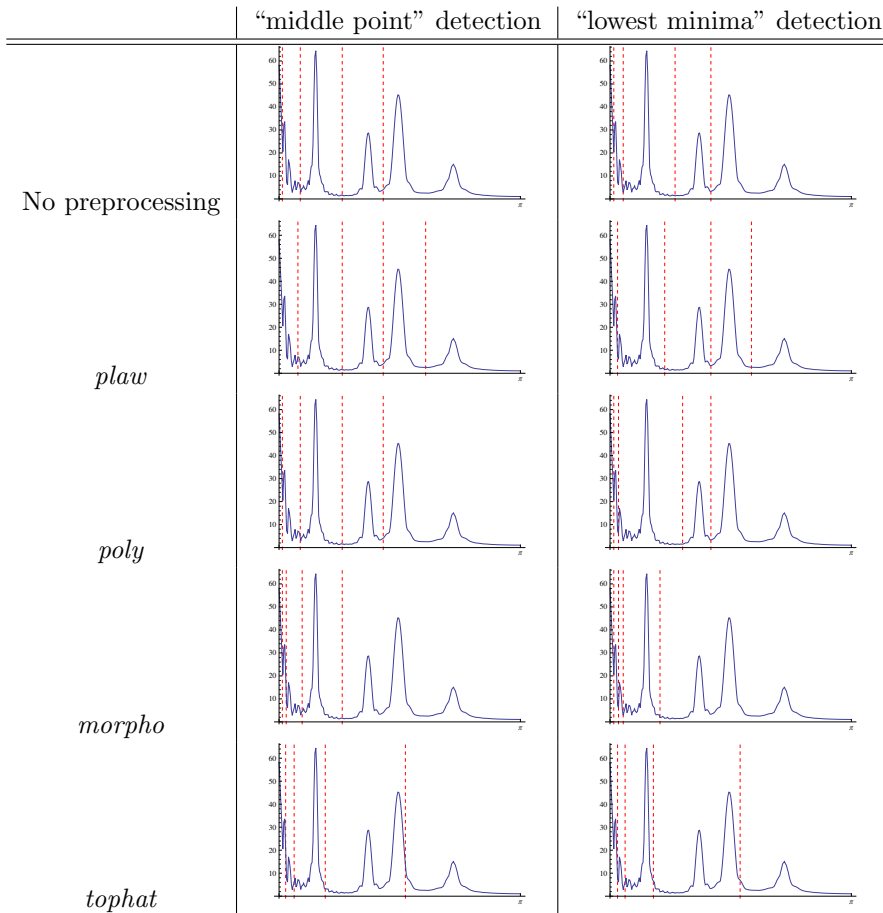


Figure 6: Fourier support detection on a spectrum with distinct modes (without any logarithm and $N = 5$). Each row correspond to different preprocessing: none, *plaw*, *poly* and *morpho*, respectively. On the left column the detection based on the middle point between consecutive maxima is shown while the right column show the results when we keep the lowest minimum between consecutive maxima.

idea is to use separately the 1D EWT on rows and columns, respectively. It is easy to see that if we consider each row (or column) independently we can obtain different sets of filters defined on very different Fourier supports. Indeed, for instance, let us consider two different rows in an image where one mainly contains edges while the other reflects the presence of textures. Their corresponding spectrum will be very different, hence providing different Fourier supports. It is possible that a scale n in one case corresponds to a completely different spectral information as opposed to the same scale from the other row. Such “discontinuity” in the filter bank leads to discontinuities in the EWT components. In order to avoid such behavior, the author proposed to use the same filter bank to process all rows and a second one to process all columns. These filters are generated by using the following procedure: for the rows, we compute

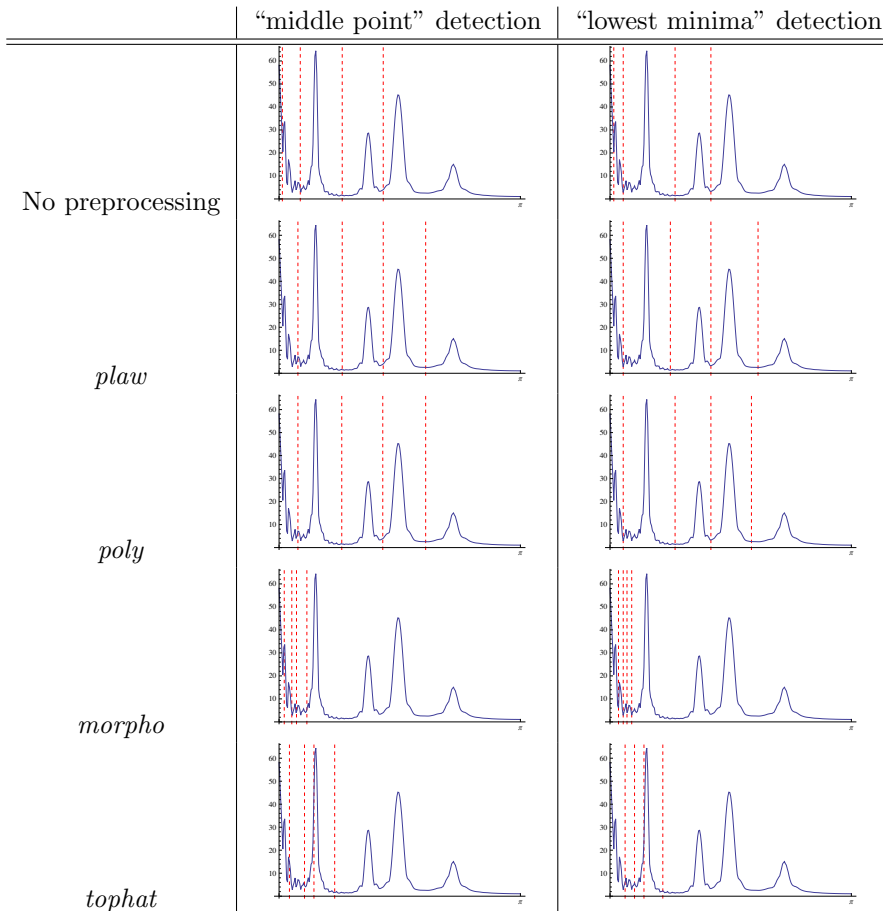


Figure 7: Fourier support detection on a spectrum with distinct modes (with applying the logarithm and $N = 5$). Each row correspond to different preprocessing: none, *plaw*, *poly* and *morpho*, respectively. On the left column the detection based on the middle point between consecutive maxima is shown while the right column show the results when we keep the lowest minimum between consecutive maxima.

the 1D FFT of each row and evaluate the average magnitude spectrum; then the Fourier supports detection is made on this average spectrum. Those supports permit us to build a unique filter bank which is used to process each row. The column case is completely equivalent by computing a column average magnitude spectrum. If we denote N_{row} and N_{col} the number of rows and columns, respectively, the 2D Tensor EWT can be resumed by Algorithm. 1.

At the end, this transform $\mathcal{W}^{\mathcal{E}\mathcal{T}}(n, m, \mathbf{x})$ provides a set of $N_R \times N_C$ subband images corresponding to a projection on the 2D frame (adopting the convention $\psi_0 = \phi_1$):

$$\mathcal{B}^{\mathcal{E}\mathcal{T}} = \left\{ \psi_{nm}(\mathbf{x}) = \psi_n^{row}(x_1) \psi_m^{col}(x_2) \right\}_{\substack{n=0, \dots, N_R-1 \\ m=0, \dots, N_C-1}} \quad (12)$$

Another point of view is that this procedure builds functions $\psi_{nm}(\mathbf{x})$ which

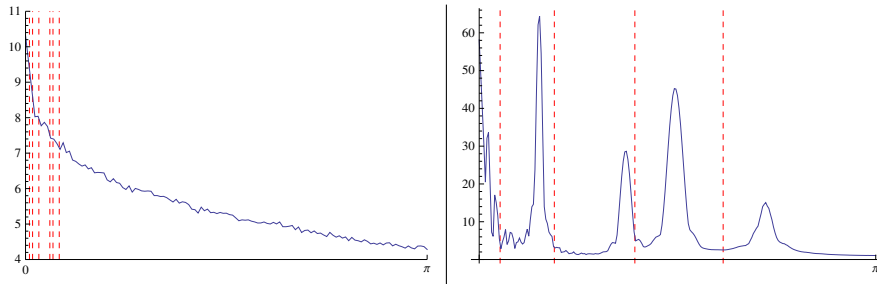


Figure 8: Fourier support detection using the Fine to Coarse algorithm.

have adaptive rectangular supports in the Fourier plane (this will be illustrated in the experiments section). The inverse transform can be obtained by using the adjoint formulation (e.g applying the inverse 1D EWT with respect to the columns first and then with respect to the rows).

5 2D Littlewood-Paley EWT

The classic 2D Littlewood-Paley wavelet transform corresponds to filter images with 2D wavelets defined in the Fourier domain on annuli supports (centered around the origin) [18]. The inner and outer radius of these supports are fixed upon a dyadic decomposition of the Fourier plane (corresponding to the usual notion of scales). It is easy to build an image for which its Fourier energy is spread into two consecutive supports leading to the separation of this information after the wavelet filtering. In this paper, we propose to apply the empirical approach to detect the radius of each annuli. The best point of view to perform this detection is to consider the Fourier plane in a polar representation because finding such boundaries is equivalent to working with the frequency modulus $|\omega|$. Some work has been made on the construction of a Pseudo-Polar FFT [1, 2] providing an operator $\mathcal{F}_P(f)(\theta, |\omega|)$. For each angle θ we have a 1D Fourier spectrum but, as in the tensor transform case, if we perform the Fourier boundaries detection for each θ independently we will introduce some discontinuities in the output components. In order to avoid such artifacts, we adapt the idea used in the tensor transform by computing an average spectrum where the averaging is taken with respect to θ : $\tilde{\mathcal{F}}(|\omega|) = \frac{1}{N_\theta} \sum_{i=0}^{N_\theta-1} \mathcal{F}_P(f)(\theta_i, |\omega|)$, where N_θ is the number of discrete angles. Then we perform the Fourier boundaries detection on $\tilde{\mathcal{F}}(|\omega|)$ and get the set of spectral radius, denoted $\{\omega^n\}_{n=0, \dots, N}$ (with $\omega^0 = 0$ and $\omega^N = \pi$), which we can use to build a set of 2D empirical Littlewood-Paley wavelets $\mathcal{B}^{\mathcal{E}\mathcal{L}\mathcal{P}} = \{\phi_1(\mathbf{x}), \{\psi_n(\mathbf{x})\}_{n=1}^{N-1}\}$. Their definition is a straightforward extension of equations (1) and (2), except for the last annuli (for $\omega^{N-1} \leq |\omega| \leq \omega^N = \pi$ where we extend the ring in order to keep the ‘‘corners’’ of the Fourier plane):

$$\mathcal{F}_2(\phi_1)(\omega) = \begin{cases} 1 & \text{if } |\omega| \leq (1 - \gamma)\omega^1 \\ \cos \left[\frac{\pi}{2} \beta \left(\frac{1}{2\gamma\omega^1} (|\omega| - (1 - \gamma)\omega^1) \right) \right] & \text{if } (1 - \gamma)\omega^1 \leq |\omega| \leq (1 + \gamma)\omega^1 \\ 0 & \text{otherwise,} \end{cases} \quad (13)$$

Algorithm 1: 2D Tensor Empirical Wavelet Transform algorithm.

- 1 **Inputs:** image $f(\mathbf{x})$, N_R (number of filters for the rows) and N_C (number of filters for the columns);
- 2 For each row i , compute its 1D FFT; $\mathcal{F}_{1,x_1}(f)(i, \omega_2)$; then compute the average row spectrum magnitude:

$$\tilde{\mathcal{F}}_{row}(\omega_2) = \frac{1}{N_{row}} \sum_{i=0}^{N_{row}-1} |\mathcal{F}_{1,x_1}(f)(i, \omega_2)|;$$

- 3 For each column j , compute its 1D FFT; $\mathcal{F}_{1,x_2}(f)(\omega_1, j)$; then compute the average row spectrum magnitude:

$$\tilde{\mathcal{F}}_{col}(\omega_1) = \frac{1}{N_{col}} \sum_{j=0}^{N_{col}-1} |\mathcal{F}_{1,x_2}(f)(\omega_1, j)|;$$

- 4 Perform the Fourier boundaries detection on $\tilde{\mathcal{F}}_{row}$ to get Ω_{row} and build $\mathcal{B}_{row} = \{\phi_1^{row}, \{\psi_n^{row}\}_{n=1}^{N_R-1}\}$ accordingly to equations (1) and (2);
 - 5 Perform the Fourier boundaries detection on $\tilde{\mathcal{F}}_{col}$ to get Ω_{col} and build $\mathcal{B}_{col} = \{\phi_1^{col}, \{\psi_m^{col}\}_{m=1}^{N_C-1}\}$ accordingly to equations (1) and (2);
 - 6 Filter f along the rows with \mathcal{B}_{row} , this provides N_R output images;
 - 7 Filter each previous output images along the columns with \mathcal{B}_{col} ;
 - 8 **Outputs:** $\mathcal{B}_{row}, \mathcal{B}_{col}, \mathcal{W}^{\mathcal{E}\mathcal{T}}(n, m, \mathbf{x})$
-

and, if $n \neq N - 1$:

$$\mathcal{F}_2(\psi_n)(\omega) = \begin{cases} 1 & \text{if } (1 + \gamma)\omega^n \leq |\omega| \leq (1 - \gamma)\omega^{n+1} \\ \cos \left[\frac{\pi}{2} \beta \left(\frac{1}{2\gamma\omega^{n+1}} (|\omega| - (1 - \gamma)\omega^{n+1}) \right) \right] & \text{if } (1 - \gamma)\omega^{n+1} \leq |\omega| \leq (1 + \gamma)\omega^{n+1} \\ \sin \left[\frac{\pi}{2} \beta \left(\frac{1}{2\gamma\omega^n} (|\omega| - (1 - \gamma)\omega^n) \right) \right] & \text{if } (1 - \gamma)\omega^n \leq |\omega| \leq (1 + \gamma)\omega^n \\ 0 & \text{otherwise,} \end{cases} \quad (14)$$

and, if $n = N - 1$:

$$\mathcal{F}_2(\psi_{N-1})(\omega) = \begin{cases} 1 & \text{if } (1 + \gamma)\omega^{N-1} \leq |\omega| \\ \sin \left[\frac{\pi}{2} \beta \left(\frac{1}{2\gamma\omega^{N-1}} (|\omega| - (1 - \gamma)\omega^{N-1}) \right) \right] & \text{if } (1 - \gamma)\omega^{N-1} \leq |\omega| \leq (1 + \gamma)\omega^{N-1} \\ 0 & \text{otherwise.} \end{cases} \quad (15)$$

Then the 2D empirical Littlewood-Paley transform of an input image f is given by

$$\mathcal{W}_f^{\mathcal{E}\mathcal{L}\mathcal{P}}(n, \mathbf{x}) = \mathcal{F}_2^* \left(\mathcal{F}_2(f)(\omega) \overline{\mathcal{F}_2(\psi_n)(\omega)} \right), \quad (16)$$

for the detail coefficients and the approximation coefficients (the convention $\mathcal{W}_f^{\mathcal{E}\mathcal{L}\mathcal{P}}(0, \mathbf{x})$ is adopted to denote them) by:

$$\mathcal{W}_f^{\mathcal{E}\mathcal{L}\mathcal{P}}(0, \mathbf{x}) = \mathcal{F}_2^* \left(\mathcal{F}_2(f)(\omega) \overline{\mathcal{F}_2(\phi_1)(\omega)} \right). \quad (17)$$

The corresponding algorithm is resumed in Algorithm. 2. The inverse transform is obtained via the adjoint formulation:

$$f(\mathbf{x}) = \mathcal{F}_2^* \left(\mathcal{F}_2(\mathcal{W}_f^{\mathcal{E}\mathcal{L}\mathcal{P}}(0, \omega) \mathcal{F}_2(\phi_1)(\omega) + \sum_{n=1}^{N-1} \mathcal{F}_2(\mathcal{W}_f^{\mathcal{E}\mathcal{L}\mathcal{P}}(n, \omega) \mathcal{F}_2(\psi_n)(\omega)) \right). \quad (18)$$

Algorithm 2: 2D Empirical Littlewood-Paley Wavelet Transform algorithm.

- 1 **Inputs:** image $f(\mathbf{x})$, N (number of filters);
- 2 Compute the Pseudo-Polar FFT, $\mathcal{F}_P(f)(\theta, |\omega|)$, and take the average with respect to θ :

$$\widetilde{\mathcal{F}}_P(|\omega|) = \frac{1}{N_\theta} \sum_{i=0}^{N_\theta-1} |\mathcal{F}_P(f)(\theta_i, |\omega|)|; \quad (19)$$

- 3 Perform the Fourier boundaries detection on $\widetilde{\mathcal{F}}_P(|\omega|)$ to get Ω and build the corresponding filter bank $\mathcal{B} = \{\phi_1(\mathbf{x}), \{\psi_n(\mathbf{x})\}_{n=1}^{N-1}\}$ accordingly to equations (13)-(15);
 - 4 Filter f by using equations (16) and (17);
 - 5 **Outputs:** $\mathcal{B}^{\mathcal{E}\mathcal{L}\mathcal{P}}$ and $\mathcal{W}_f^{\mathcal{E}\mathcal{L}\mathcal{P}}(n, \mathbf{x})$
-

6 Empirical Ridgelet Transform

The ridgelet transform was introduced by Candès and Donoho [7, 8, 16] and was one of the first directional 2D wavelet type transforms. The idea is to consider the usual wavelet transform on a collection of 1D signals. This 1D signal collection is generated by an inverse 1D FFT of the 1D spectrum profile extracted from the 2D FFT of the input image along lines going through the origin and with angle θ . By using our notations, the classical ridgelet transform can be written, $0 < n < N$ (where $n = 0$ corresponds to the approximation subband),

$$\mathcal{W}_f^{\mathcal{R}}(n, \theta, t) = \mathcal{W}_{1,t}(\mathcal{F}_{1,|\omega|}^*(\mathcal{F}_P(f)(\theta, |\omega|))), \quad (20)$$

and its inverse

$$f(\mathbf{x}) = \mathcal{F}_P^*(\mathcal{F}_{1,t}(\mathcal{W}_{1,t}^*(\mathcal{W}_f^{\mathcal{R}}))). \quad (21)$$

We can define the empirical ridgelet transform by the same algorithm except that we replace the standard 1D wavelet transform by the 1D empirical wavelet transform. Note that in this case the number of subbands is supposed to depend on θ which means that we will face the same discontinuity problems as for the tensor or Littlewood-Paley approaches. One more time, in order to avoid

such issue, we will use the same method as for the Littlewood-Paley algorithm: we will detect the Fourier boundaries on an average spectrum (with respect to θ) obtained from the Pseudo-Polar FFT. Then we build the set $\mathcal{B}^{\mathcal{ER}} = \{\phi_1(t), \{\psi_n(t)\}_{n=1}^{N-1}\}$ which will be used to perform the 1D EWT. Hence the empirical ridgelet transform is defined by ($\mathcal{W}_t^{\mathcal{E}}$ is the 1D EWT based on \mathcal{B} with respect to t)

$$\mathcal{W}_f^{\mathcal{ER}}(n, \theta, t) = \mathcal{W}_t^{\mathcal{E}}(\mathcal{F}_{1,\omega}^*(\mathcal{F}_P(f))), \quad (22)$$

and its inverse

$$f(\mathbf{x}) = \mathcal{F}_P^*(\mathcal{F}_{1,t}(\mathcal{W}_t^{\mathcal{E}*}(\mathcal{W}_f^{\mathcal{ER}}))). \quad (23)$$

Because the empirical wavelet is defined in the Fourier domain, we can simplify these equations to

$$\mathcal{W}_f^{\mathcal{ER}}(n, \theta, t) = \mathcal{F}_{1,\omega}^* \left(\mathcal{F}_P(f)(\omega, \theta) \overline{\mathcal{F}_{1,t}(\psi_n)(\omega)} \right), \quad (24)$$

$$\mathcal{W}_f^{\mathcal{ER}}(0, \theta, t) = \mathcal{F}_{1,\omega}^* \left(\mathcal{F}_P(f)(\omega, \theta) \overline{\mathcal{F}_{1,t}(\phi_1)(\omega)} \right), \quad (25)$$

and its inverse

$$f(\mathbf{x}) = \mathcal{F}_P^* \left(\mathcal{F}_{1,t}(\mathcal{W}_f^{\mathcal{ER}}(0, \theta, t)) \mathcal{F}_{1,t}(\phi_1)(\omega) + \sum_{n=1}^{N-1} \mathcal{F}_{1,t}(\mathcal{W}_f^{\mathcal{ER}}(n, \theta, t)) \mathcal{F}_{1,t}(\psi_n)(\omega) \right). \quad (26)$$

The corresponding algorithm is resumed in Algorithm. 3.

Algorithm 3: Empirical Ridgelet Transform algorithm.

- 1 **Inputs:** image $f(\mathbf{x})$, N (number of filters);
- 2 Compute the Pseudo-Polar FFT, $\mathcal{F}_P(f)(\theta, |\omega|)$, and take the average with respect to θ :

$$\widetilde{\mathcal{F}}_P(|\omega|) = \frac{1}{N_\theta} \sum_{i=0}^{N_\theta-1} |\mathcal{F}_P(f)(\theta_i, |\omega|)|; \quad (27)$$

- 3 Perform the Fourier boundaries detection on $\widetilde{\mathcal{F}}_P(|\omega|)$ to get Ω and build the corresponding filter bank $\mathcal{B}^{\mathcal{ER}} = \{\phi_1(\mathbf{x}), \{\psi_n(\mathbf{x})\}_{n=1}^{N-1}\}$ accordingly to equations (1)-(2);
 - 4 Filter f by using equations (24) and (25);
 - 5 **Outputs:** $\mathcal{B}^{\mathcal{ER}}$ and $\mathcal{W}_f^{\mathcal{ER}}(n, \theta, t)$
-

7 Empirical Curvelet Transform

The curvelet transform was introduced by Candès et al. in [9, 10, 11]. The concept behind this transform is to build a filter bank in the Fourier domain where each filter has its support located on a ‘‘polar wedge’’. The Fourier transform of one curvelet can be written $((\omega, \theta)$ are the polar coordinates in the Fourier plane) as $\mathcal{F}_2(\psi_j)(\omega, \theta) = 2^{-3j/4} W(2^{-j}\omega) V\left(\frac{2^{\lfloor j/2 \rfloor} \theta}{2\pi}\right)$ where $W(r)$ and $V(t)$ (called the radial window and the angular window, respectively) are smooth, nonnegative

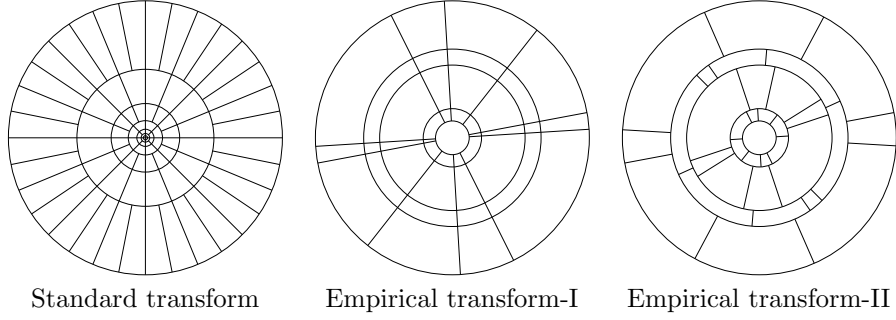


Figure 9: Curvelet tiling of the Fourier plane.

and real-valued functions defined over compact supports (with $r \in (1/2, 2)$ and $t \in [-1, 1]$). A dyadic decomposition is used to partition the Fourier plane: the low frequencies are located on a disk centered at the zero frequency and each scale are defined on concentric annuli (in the same idea as the Littlewood-Paley transform), the angle ranges corresponding to each angular sector are also split into dyadic intervals and their number double every two scales (see left diagram on Figure. 9). The empirical extension will consist in both empirically detect the scales and the angles corresponding to each polar wedge. We assume that the number of scales N_s and the number of angular sectors N_θ are given. The detection process provides us with a set of scale boundaries $\Omega_\omega = \{\omega^n\}_{n=0, \dots, N_s}$ and a set of angular boundaries $\Omega_\theta = \{\theta^m\}_{m=1, \dots, N_\theta}$. The (purely radial) low-pass filter ϕ_1 is equivalent to the one used in the Littlewood-Paley transform and is given by Equation. 13. As with the standard curvelets, a polar wedge ψ_{nm} (n and m are the scale and angular indices, respectively) in the Fourier domain is the product of a radial window, W_n , which for $n \neq N_s - 1$ is given

$$W_n(\omega) = \begin{cases} 1 & \text{if } (1 + \gamma)\omega^n \leq |\omega| \leq (1 - \gamma)\omega^{n+1} \\ \cos \left[\frac{\pi}{2} \beta \left(\frac{1}{2\gamma\omega^{n+1}} (|\omega| - (1 - \gamma)\omega^{n+1}) \right) \right] & \text{if } (1 - \gamma)\omega^{n+1} \leq |\omega| \leq (1 + \gamma)\omega^{n+1} \\ \sin \left[\frac{\pi}{2} \beta \left(\frac{1}{2\gamma\omega^n} (|\omega| - (1 - \gamma)\omega^n) \right) \right] & \text{if } (1 - \gamma)\omega^n \leq |\omega| \leq (1 + \gamma)\omega^n \\ 0 & \text{otherwise.} \end{cases} \quad (28)$$

and, if $n = N_s - 1$:

$$W_{N_s-1}(\omega) = \begin{cases} 1 & \text{if } (1 + \gamma)\omega^{N_s-1} \leq |\omega| \\ \sin \left[\frac{\pi}{2} \beta \left(\frac{1}{2\gamma\omega^{N_s-1}} (|\omega| - (1 - \gamma)\omega^{N_s-1}) \right) \right] & \text{if } (1 - \gamma)\omega^{N_s-1} \leq |\omega| \leq (1 + \gamma)\omega^{N_s-1} \\ 0 & \text{otherwise.} \end{cases} \quad (29)$$

and a polar window, V_m ,

$$V_m(\theta) = \begin{cases} 1 & \text{if } \theta^m + \Delta\theta \leq \theta \leq \theta^{m+1} - \Delta\theta \\ \cos \left[\frac{\pi}{2} \beta \left(\frac{1}{2\Delta\theta} (\theta - \theta^{m+1} + \Delta\theta) \right) \right] & \text{if } \theta^{m+1} - \Delta\theta \leq \theta \leq \theta^{m+1} + \Delta\theta \\ \sin \left[\frac{\pi}{2} \beta \left(\frac{1}{2\Delta\theta} (\theta - \theta^m + \Delta\theta) \right) \right] & \text{if } \theta^m - \Delta\theta \leq \theta \leq \theta^m + \Delta\theta \\ 0 & \text{otherwise.} \end{cases} \quad (30)$$

where $\theta^{N_\theta+1} = \theta^1 + \pi$ and (ω, θ) are the polar coordinates in the Fourier plane. Moreover, in this paper, we only consider real transforms i.e. these filters are symmetric about the origin. This leads us to the construction of the set $\mathcal{B}_I^{\mathcal{E}\mathcal{C}} = \left\{ \phi_1(\mathbf{x}), \{\psi_{nm}(\mathbf{x})\}_{\substack{n=1\dots N_s-1 \\ m=1\dots N_\theta}} \right\}$ but other options are possible. Indeed the previous definition of $\mathcal{B}_I^{\mathcal{E}\mathcal{C}}$ consider the case where the scales and angles are detected independently. It is also possible to consider that one detection depends on the other. For instance, we can detect first the scales Ω_ω and then detect different angles sets Ω_θ^ω for each scale (the other case is to detect first the angles and then the scales for each angular sector, but this case will lead to some information discontinuities from one angular sector to its neighbours and will not be considered in this paper). In this case we then build a set $\mathcal{B}_{II}^{\mathcal{E}\mathcal{C}} = \left\{ \phi_1(\mathbf{x}), \{\psi_{nm}(\mathbf{x})\}_{\substack{n=1\dots N_s-1 \\ m=1\dots N_\theta}} \right\}$ where the angular window is dependent of n because based on Ω_θ^ω instead of Ω_θ (concretely, the bounds θ^m depend on n : θ_n^m).

8 Frame properties

The following theorem gives the conditions such that all each previous transform are tight frames of L^2 .

Theorem 1 *Let $\mathcal{B}^{\mathcal{E}\mathcal{T}}$, $\mathcal{B}^{\mathcal{E}\mathcal{L}\mathcal{P}}$, $\mathcal{B}^{\mathcal{E}\mathcal{R}}$, $\mathcal{B}_I^{\mathcal{E}\mathcal{C}}$ and $\mathcal{B}_{II}^{\mathcal{E}\mathcal{C}}$ be the families of wavelets described in the previous sections. If their corresponding parameters γ and $\Delta\theta$ (for the curvelet transforms) are chosen in order to avoid any overlapping of the transition areas (both for scales and angles) then these families are tight frames of L^2 .*

Proof 1 *Let us start with the tensor product transform. Because of the tensor product properties we have $\mathcal{F}(\psi_{nm})(\omega) = \mathcal{F}(\psi_n^{row})(\omega_1)\mathcal{F}(\psi_n^{col})(\omega_2)$. Then*

$$\begin{aligned} \sum_n \sum_m |\mathcal{F}(\psi_{nm})(\omega)|^2 &= \sum_n \sum_m |\mathcal{F}(\psi_n^{row})(\omega_1)|^2 |\mathcal{F}(\psi_n^{col})(\omega_2)|^2 \\ &= \left(\sum_n |\mathcal{F}(\psi_n^{row})(\omega_1)|^2 \right) \left(\sum_m |\mathcal{F}(\psi_n^{col})(\omega_2)|^2 \right). \end{aligned} \quad (31)$$

But each term can be viewed as a 1D empirical wavelet set which we know from [17] that if γ is properly chosen then $\sum_n |\mathcal{F}(\psi_n^{row})(\omega_1)|^2 = \sum_n |\mathcal{F}(\psi_n^{col})(\omega_2)|^2 = 1$. Finally we get $\sum_n \sum_m |\mathcal{F}(\psi_{nm})(\omega)|^2 = 1$ which end the tensor product case.

The Littlewood-Paley case is straightforward because it is a radial function defined from the 1D empirical wavelet which directly inherits its properties.

The ridgelet case is also straightforward as it corresponds to take 1D EWT along lines at different angles.

Let us address now the curvelet cases. We start from the first option when scales and angles are independently detected. In this case, we have $|\mathcal{F}(\phi_1)(\omega)|^2 + \sum_n \sum_m |\mathcal{F}(\psi_{nm}(\omega))|^2 = |\mathcal{F}(\phi_1)(\omega)|^2 + \sum_n \sum_m |W_n(\omega)|^2 |V_m(\theta)|^2 = |\mathcal{F}(\phi_1)(\omega)|^2 + \sum_n |W_n(\omega)|^2 \sum_m |V_m(\theta)|^2$. But by construction (it is the same concept as the low pass filters $\mathcal{F}(\phi_1)$) we have $\sum_m |V_m(\theta)|^2 = 1$ and then $|\mathcal{F}(\phi_1)(\omega)|^2 + \sum_n |W_n(\omega)|^2$ returns us to the Littlewood-Paley case. The second curvelet case is almost equivalent except that now the angular tiling depends on each scale which is equivalent to study $|\mathcal{F}(\phi_1)(\omega)|^2 + \sum_n (|W_n(\omega)|^2 \sum_m |V_m^n(\theta)|^2)$. One more time, if we consider a fixed scale n , by construction we have $\sum_m |V_m^n(\theta)|^2 = 1$ and we conclude with the same argument as the first case.

9 Experiments

9.1 Transform examples

In this section we illustrate the output components obtained from the previously described empirical transforms. The tests are made on two different images. The first one is a toy example containing some flat objects as well as different textures lying at different scales and orientations, this image and its Fourier spectrum are given in figure. 10. The second image is the classic Lena image, see figure. 11 for the image and its Fourier spectrum. Figures. 12 and 13 present the coefficients obtained from the tensor transform approach. The corresponding Fourier supports are given in the top row of Figure. 18, we can see that the detection performs relatively differently with respect to the horizontal and vertical directions. Coefficients obtained from the 2D Littlewood-Paley transform are shown on Figures. 14 and 15, respectively, while the corresponding detected annuli are given in the bottom row of Figure. 18. Figures 16 and 17 present the ridgelet coefficients (the Fourier boundaries correspond to the Littlewood-Paley case) while Figures. 19, 20, 21 and 22 show the curvelet coefficients for each option. The corresponding tiling are given in Figure. 23. For the toy example, it is clear that the Fourier supports for each transform try to separate the different modes.

9.2 Denoising

In order to have some intuition on the applicability of the proposed transforms, in this section, we present some denoising experiments. The used denoising method consists in three simple steps: we perform the transform of a noisy image, then we apply a soft thresholding on the obtained coefficients and finally we perform the inverse transform to get the denoised image. This method is not the best denoising method in the literature but it is sufficient to get some clues on the proposed transforms. The noisy images are built from the toy and Lena images, mentioned in the previous section, on which we add an additive Gaussian noise. The used threshold is given by $\delta\sqrt{2\log N_p}$, where N_p is the number of pixels and δ is a tuning parameter, optimized on each experiment to

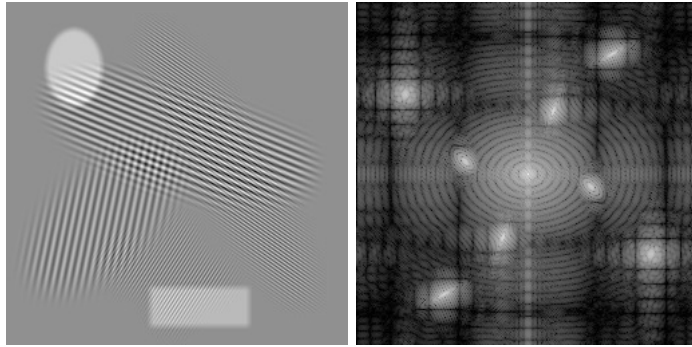


Figure 10: Toy image and the logarithm magnitude of its Fourier spectrum.



Figure 11: Lena image and the logarithm magnitude of its Fourier spectrum.

get the best denoising results. To compare the denoising efficiency, we compute two different metrics (the reference image is denoted I_r and the denoised image I_d):

- the usual PSNR (Peak Signal to Noise Ratio), defined by $PSNR = 10 \log_{10} \left(\frac{Max^2}{MSE} \right)$, where Max is the maximum possible value in the image and $MSE = \frac{1}{N_P} \|I_r - I_d\|_2^2$,
- the SSIM (Structural Similarity Index Measure [30]), this metric is more consistent with the human eye perception than the PSNR. This metric is defined by

$$SSIM = \frac{(2\mu_r\mu_d + c_1)(2\sigma_{rd} + c_2)}{(\mu_r^2 + \mu_d^2 + c_1)(\sigma_r^2 + \sigma_d^2 + c_2)},$$

where μ_r, μ_d are the averages of I_r and I_d and $\sigma_r, \sigma_d, \sigma_{rd}$ the variances and covariance of I_r and I_d , respectively. The constants c_1 and c_2 are defined by $c_1 = (0.01L)^2$ and $c_2 = (0.03L)^2$ where L is the dynamic range (see [30] for full details).

In order to get a good intuition, we also perform the same denoising technique with the classic wavelet, ridgelet and curvelet transforms. The corresponding results are given in Table. 1. Even though this table shows that the classic

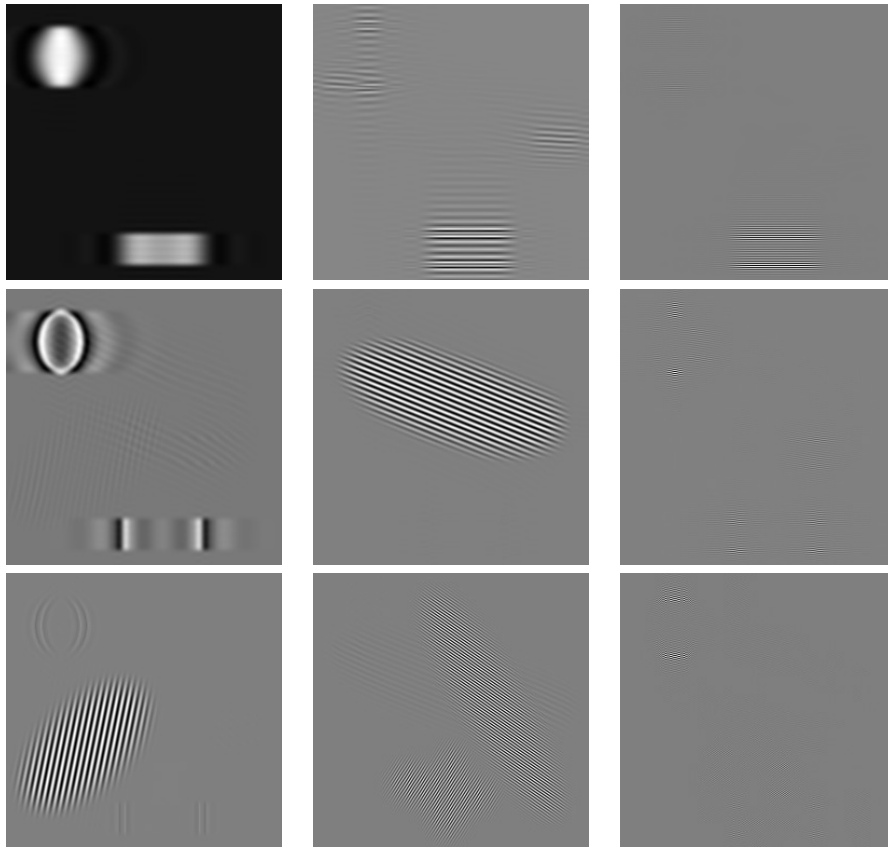


Figure 12: 2D Tensor EWT components of the toy image ($N_R = 3, N_C = 3$, the logarithm, the *morpho* preprocessing and the lowest minima detection are used).

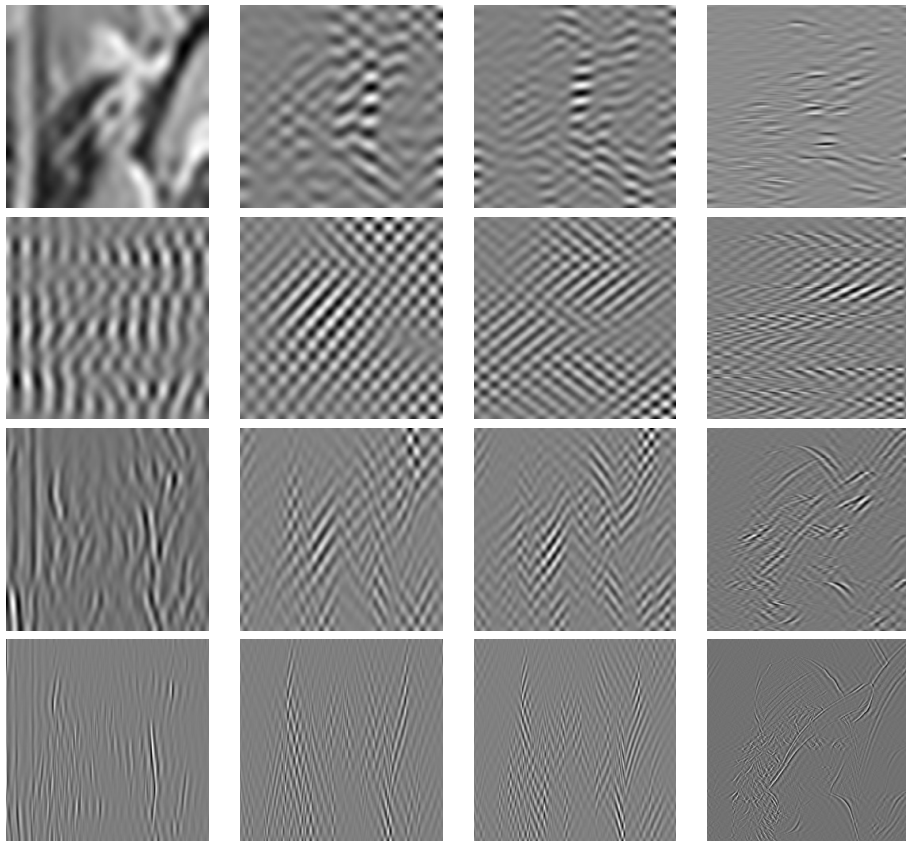


Figure 13: 2D Tensor EWT components of the Lena image ($N_R = 4, N_C = 4$, the logarithm, the *morpho* preprocessing and the lowest minima detection are used).

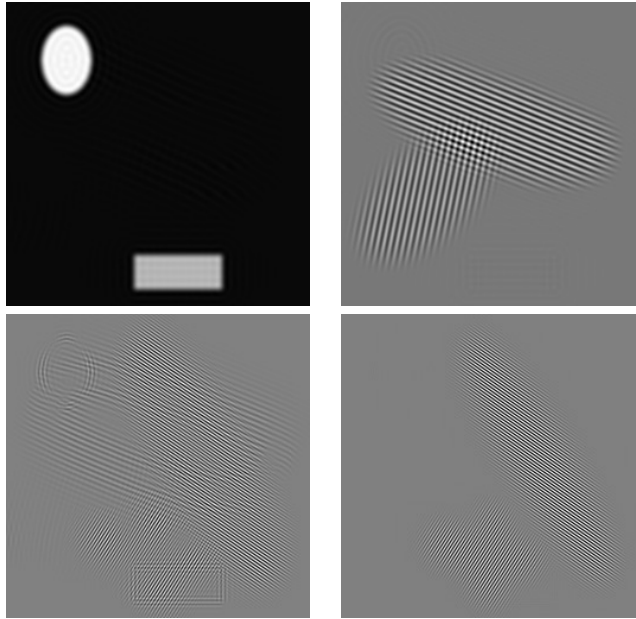


Figure 14: 2D Littlewood-Paley EWT components of the toy image ($N = 4$, the logarithm, the *morpho* preprocessing and the lowest minima detection are used).

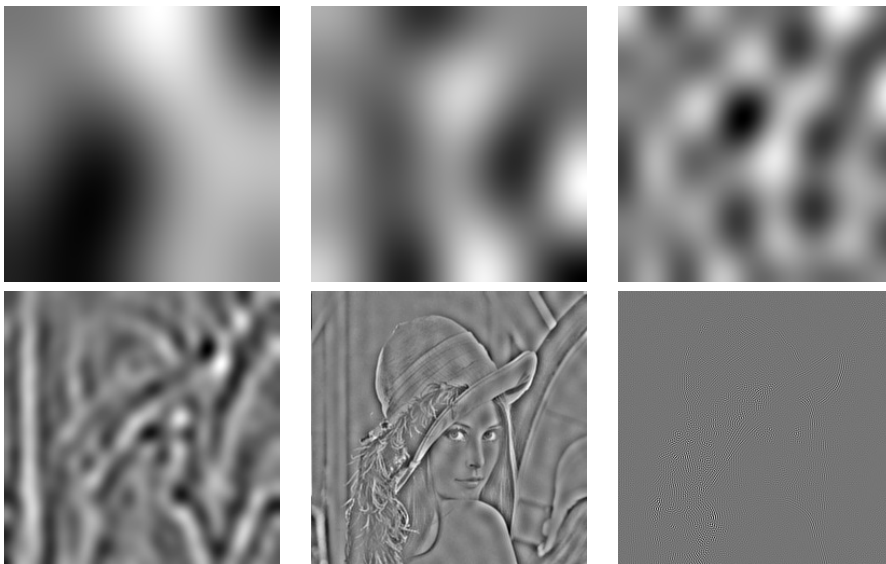


Figure 15: 2D Littlewood-Paley EWT components of the Lena image ($N = 6$, the logarithm, the *morpho* preprocessing and the lowest minima detection are used).

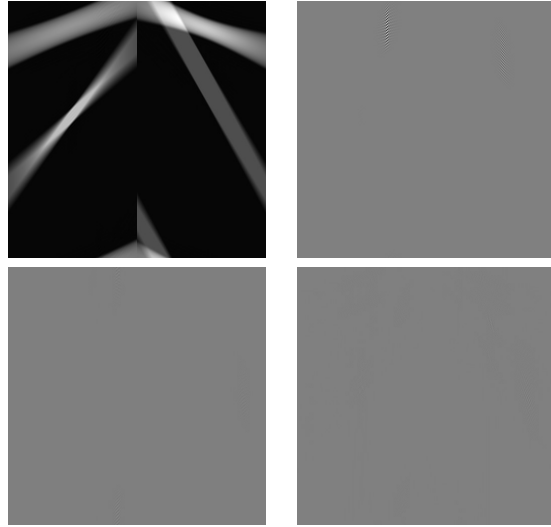


Figure 16: Empirical ridgelet components of the toy image ($N = 4$).

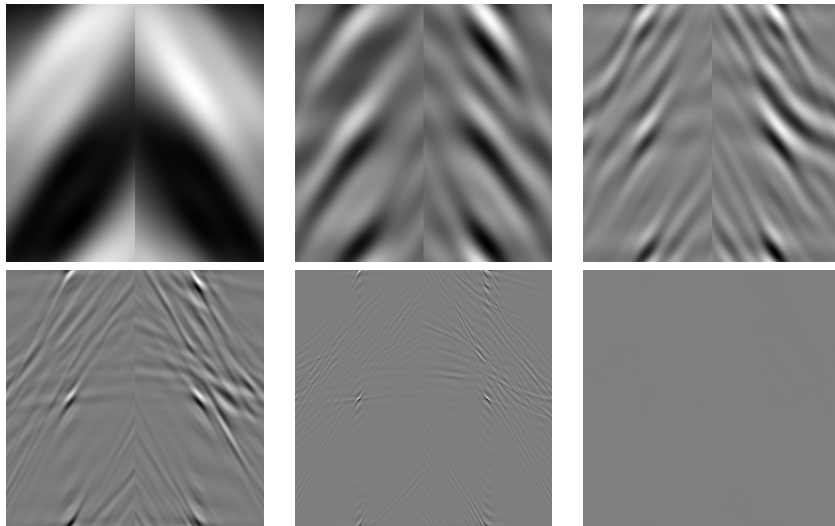


Figure 17: Empirical ridgelet components of the Lena image ($N = 6$).

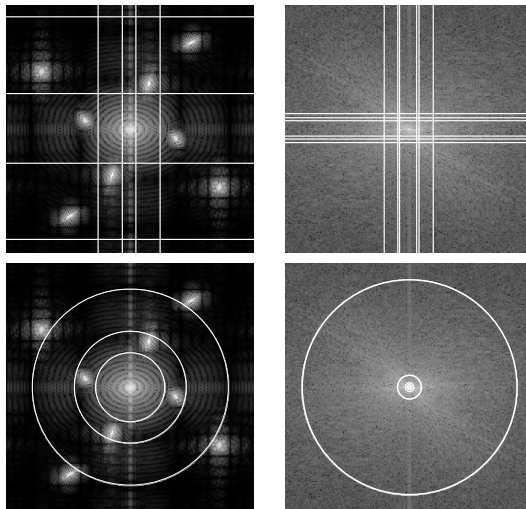


Figure 18: Detected Fourier boundaries for each test image (toy image on left and Lena on right). Tensor EWT approach on top and Littlewood-Paley/Ridgelet approaches on bottom.

curvelet transform outperforms all the other ones, it is interesting to note that, in the case of the toy image, the empirical ridgelet and curvelet transforms provide better results (in terms of SSIM) than the classic wavelet and ridgelet transforms. Surprisingly, on Lena, the empirical tensor wavelet transform is the best empirical approach (and even beats the classic ridgelet transform). If these experiments do not give the empirical approach as the best ones, they show that the empirical methods can behave totally differently accordingly to the kind of processed image. These results lead us to think that it should be interesting to use a more advanced denoising method like considering different thresholds adapted to each subbands or finding the image which have the sparsest representation in each transform domain by solving an $L^1 - L^2$ problem like in [27].

10 Conclusion

In this paper, we extend the 1D Empirical Wavelet Transform proposed in [17] to the 2D case. Thus we revisit the tensor wavelet transform, the 2D Littlewood-Paley transform, the ridgelet transform and the curvelet transform and their inverses. We show that it is possible to build adaptive wavelet frames which are pretty flexible to use in practice. We also propose different options concerning how to perform the Fourier boundary detection. It is clear that depending on how this detection task is performed the corresponding expansions can be very different. This step is probably the most important step in these empirical transforms. Experiments seem to show that the algorithm used to do this detection depends on the final goal and the type of analyzed image. Indeed, we will not chose the same algorithm if the Fourier spectrum has or not clearly distinct modes.

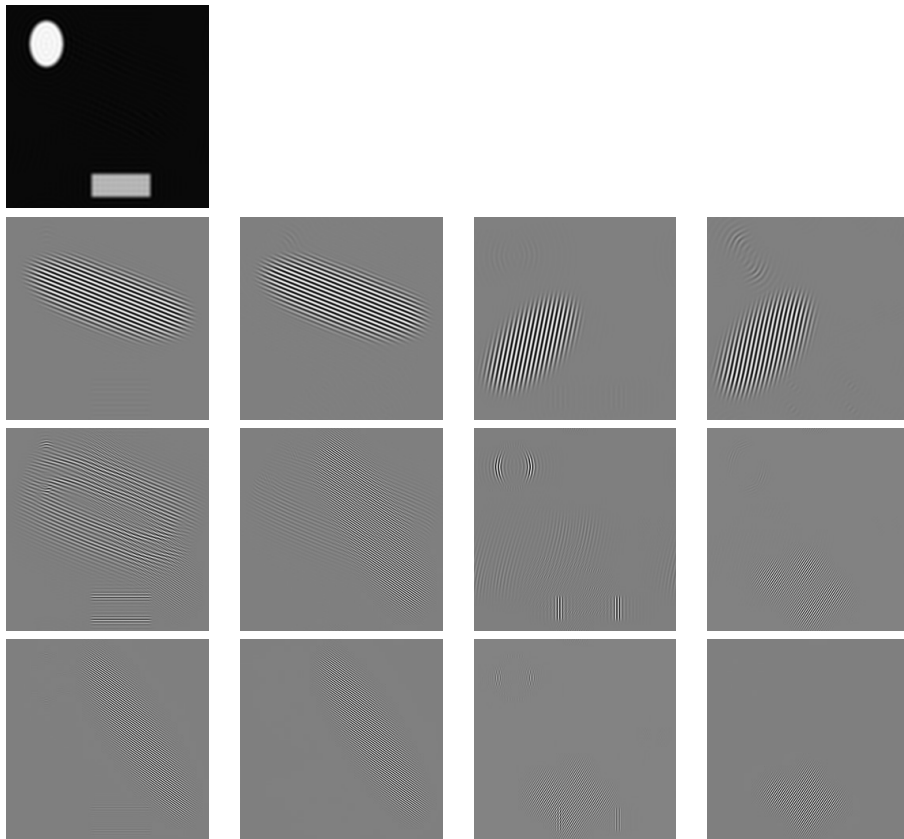


Figure 19: 2D Curvelet EWT-I components of the toy image ($N_s = 4, N_\theta = 4$, the logarithm, the *morpho* preprocessing and the lowest minima detection are used to detect the scales and middle between local maxima with *tophat* are used to detect the angles).

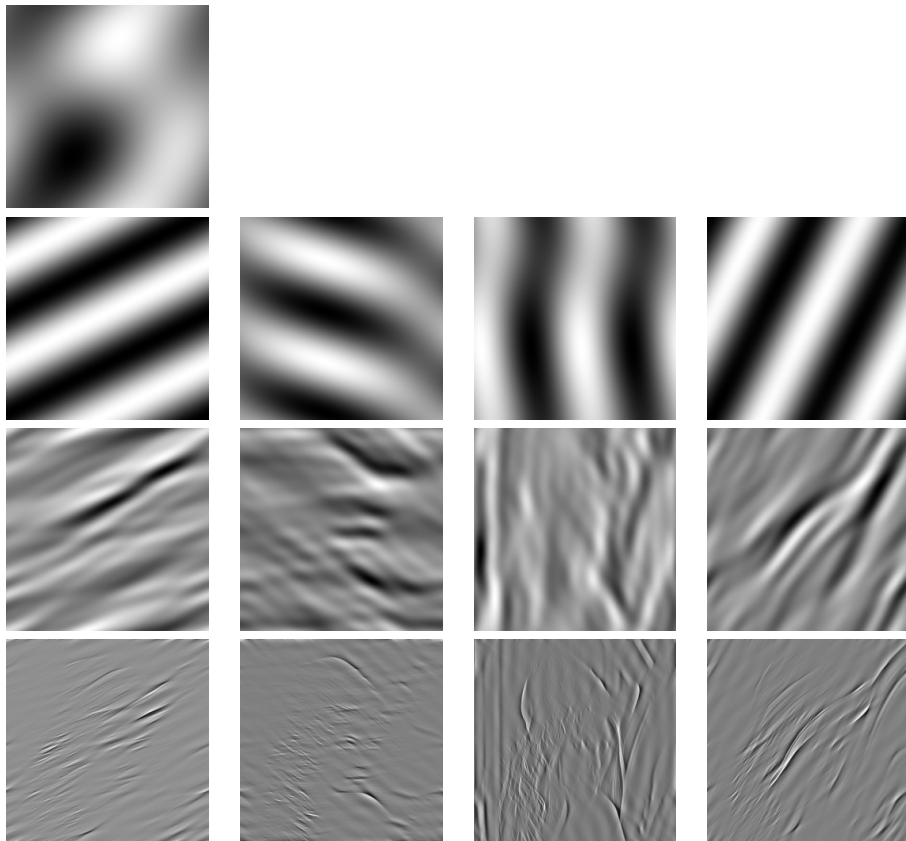


Figure 20: 2D Curvelet EWT-I components of the Lena image ($N_s = 4, N_\theta = 4$, the logarithm, the *morpho* preprocessing and the lowest minima detection are used to detect the scales and middle between local maxima with *tophat* are used to detect the angles).

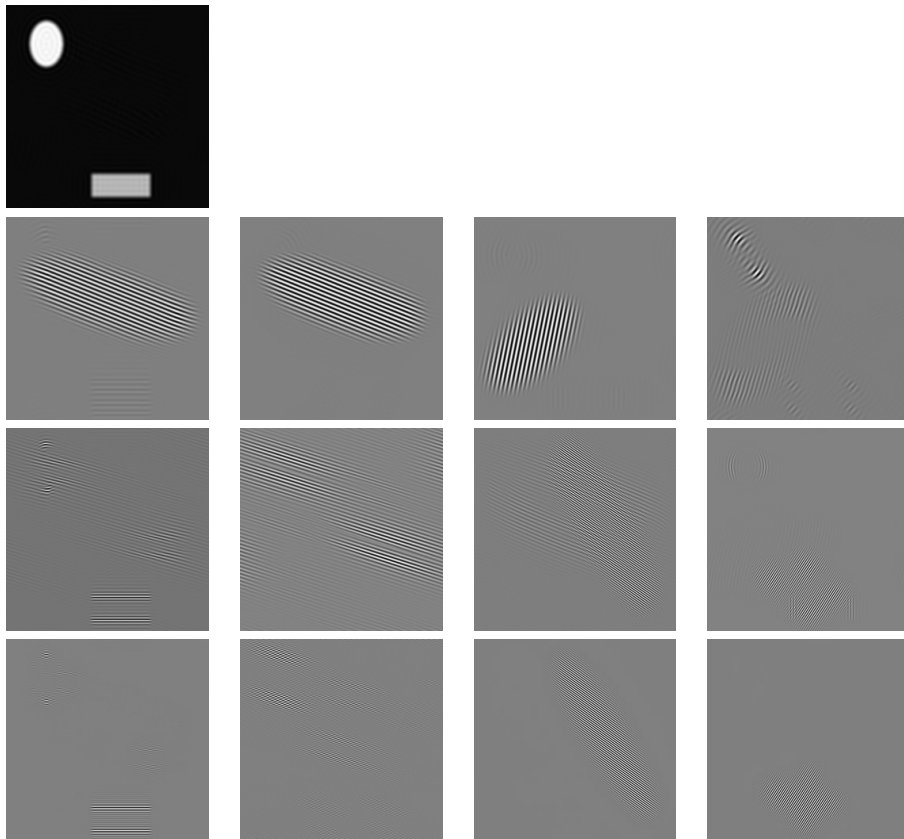


Figure 21: 2D Curvelet EWT-II components of the toy image ($N_s = 4, N_\theta = 4$, the logarithm, the *morpho* preprocessing and the lowest minima detection are used to detect the scales and middle between local maxima with *tophat* are used to detect the angles).

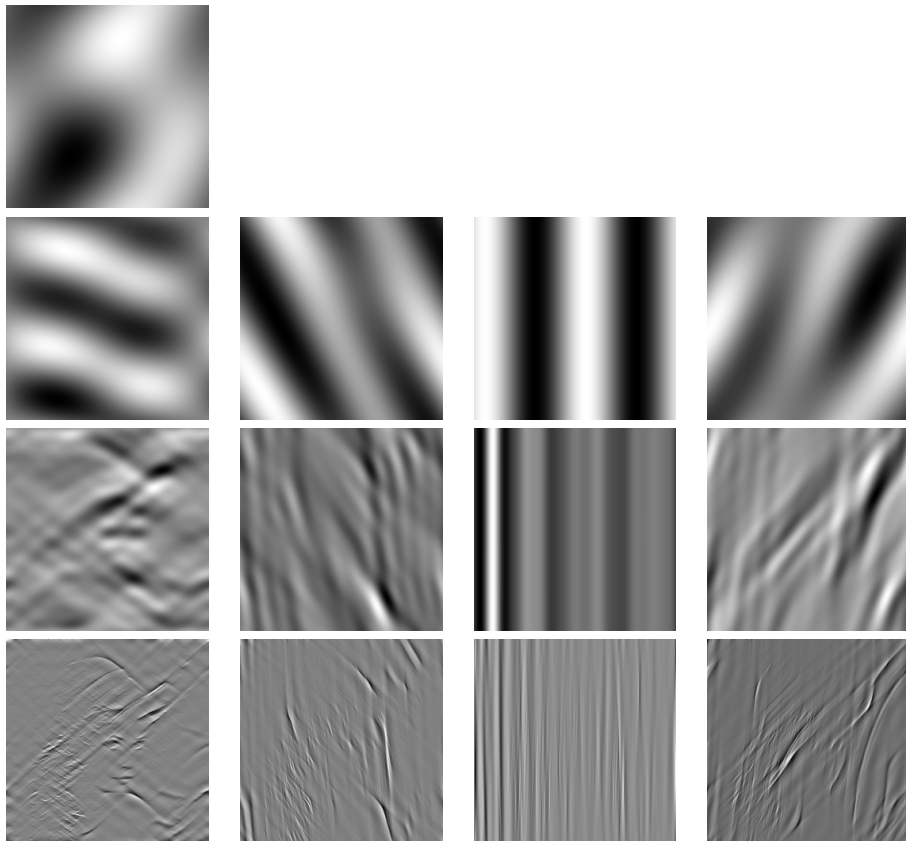


Figure 22: 2D Curvelet EWT-II components of the Lena image ($N_s = 4, N_\theta = 4$, the logarithm, the *morpho* preprocessing and the lowest minima detection are used to detect the scales and middle between local maxima with *tophat* are used to detect the angles).

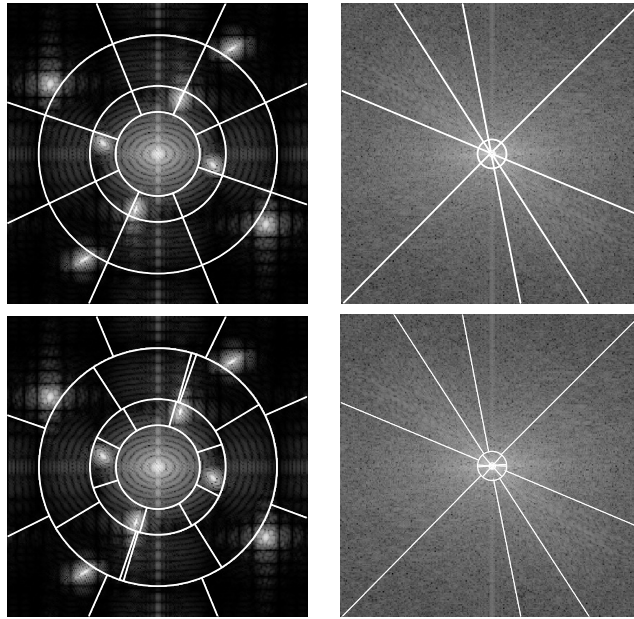


Figure 23: Detected Fourier boundaries for each test image (toy image on left and Lena on right). Curvelet EWT-I approach on top and Curvelet EWT-II approach on bottom.

Table 1: Denoising results (noise variance: $\sigma = 10$ for Lena and $\sigma = 1$ for the toy image).

	Lena		Toy image	
	PSNR	SSIM	PSNR	SSIM
Noisy	28.096956	0.709367	48.143956	0.456469
Wavelet	31.151106	0.876431	52.365411	0.678816
Ridgelet	29.018199	0.811983	55.038634	0.708038
Curvelet	31.762547	0.9019	58.977812	0.928533
EWT Tensor	28.956752	0.821412	52.480827	0.648255
EWT Ridgelet	9.610751	0.744987	57.10384	0.821604
EWT Curvelet I	16.253502	0.781414	52.79413	0.712689
EWT Curvelet II	19.802442	0.769585	52.366085	0.740332

On the practical side, these transforms provide sparse representations of images which could be used for restoration purposes (denoising, deblurring for instance). We present some denoising results based on a very simple approach, which do not give the advantage to the empirical transforms but lead us to think that more advanced denoising methods, like the ones presented in [4, 5, 6], must be investigated. Such study will be presented in a future work.

Another extension of this work should be the opportunity to perform a true 2D segmentation of the Fourier spectrum and then build 2D wavelets on the

obtained partitioning. If this idea seems reasonable, it opens some challenging questions like: how to efficiently perform such segmentation? How to build such wavelet on arbitrary supports?

11 Acknowledgement

This work is partially funded by the following grants NSF DMS-0914856, NSF DMS-1118971, ONR N00014-08-1-1119, ONR N0014-09-1-0360, ONR MURI USC, the UC Lab Fees Research and the Keck Foundation.

A Pseudo-Polar Fourier Transform

The polar Fourier transform is a useful tool for applications like tomography, radon transform computations or in the definition of the ridgelet transform. In [1], the authors propose a fast algorithm to compute the Pseudo-Polar Fourier transform where the polar frequency points are not defined on a regular grid but on a pseudo grid like the one depicted in Figure. 24. Providing the frequencies (ω_1, ω_2) sampled on this pseudo grid, and assuming that the input image f has $N \times N$ pixels, the pseudo-polar Fourier transform is defined by

$$\mathcal{F}_P(f)(\omega_1, \omega_2) = \sum_{x_1=0}^{N-1} \sum_{x_2=0}^{N-1} f(x_1, x_2) \exp(-i(x_1\omega_1 + x_2\omega_2)). \quad (32)$$

The inverse transform is performed by a least square minimization scheme. Providing a pseudo-polar Fourier transform f_P of an image f , a gradient descent is used to perform

$$f = \arg \min_x \|\mathcal{F}_P(x) - f_P\|_2^2. \quad (33)$$

See [1] for all numerical details. The authors freely provide a Matlab implementation of this algorithm.

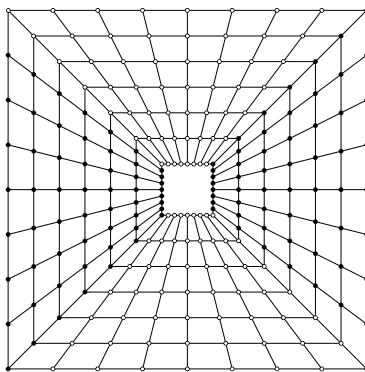


Figure 24: Pseudo-polar grid.

B Mathematical morphology operators

In the boundary detection section (3), we used some mathematical morphological operators that we recall in this appendix. The two basic operators are the dilation (*Dil*) and erosion (*Er*), they are respectively defined by

$$Dil(f, b)(x) = \sup_y (f(y) + b(x - y)) \quad ; \quad Er(f, b)(x) = \inf_y (f(y) - b(x - y)), \quad (34)$$

where the function b is called the structuring function. It is usual in the literature to consider flat structuring functions: $b(x) = 0$ if $x \in B$ and $b(x) = -\infty$ otherwise. Then the dilation and erosion operators resumed to

$$Dil(f, b)(x) = \sup_{y-x \in B} (f(y)) \quad ; \quad Er(f, b)(x) = \inf_{y-x \in B} (f(y)), \quad (35)$$

the only remaining parameter is the size of the support B . From these two basic operators, we can define the opening and closing operators:

$$Cl(f, b) = Er(Dil(f, b), b) \quad ; \quad Op(f, b) = Dil(Er(f, b), b). \quad (36)$$

Basically, the closing operator “fills” holes smaller than the structuring function while the opening operator remove spikes smaller than the structuring function.

References

- [1] A. AVERBUCH AND R.R. COIFMAN AND D.L. DONOHO AND M. ELAD AND M. ISRAELI, *Fast and accurate Polar Fourier transform*, Applied and Computational Harmonic Analysis, Vol. 21, pp. 145–167, 2006.
- [2] A. AVERBUCH AND R.R. COIFMAN AND D.L. DONOHO AND M. ISRAELI AND Y. SHKOLNISKY, *A Framework for Discrete Integral Transformations I-The Pseudopolar Fourier Transform*, SIAM Journal on Scientific Computing, Vol. 30, No. 2, pp. 764–784, 2008.
- [3] L. BORUP AND M. NIELSEN, *Approximation with brushlet systems*, Journal of Approximation Theory, Vol. 123, pp. 25–51, 2003.
- [4] J-F. CAI AND H. JI AND C-Q. LIU AND Z. SHEN, *Blind motion deblurring from a single image using sparse approximation*, IEEE Conference on Computer Vision and Pattern Recognition (CVPR), Miami, 2009.
- [5] J-F. CAI AND S. OSHER AND Z. SHEN, *Linearized Bregman Iterations for Frame-Based Image Deblurring*, SIAM Journal on Imaging Sciences, Vol. 2, No. 1, pp. 226–252, 2009.
- [6] J-F. CAI AND S. OSHER AND Z. SHEN, *Split Bregman Methods and Frame Based Image Restoration*, SIAM Journal on Multiscale Modeling and Simulation, Vol. 8, No. 2, pp. 337–369, 2009.
- [7] E.J. CANDÈS, *Ridgelets: estimating with ridge functions*, The Annals of Statistics, Vol. 31, No. 5, pp. 1561-1599, 2003.
- [8] E.J. CANDÈS, *Ridgelets: Theory and Applications*, Ph.D Thesis, Department of Statistics, Stanford University, 1998.
- [9] E.J. CANDÈS AND D.L. DONOHO, *Continuous Curvelet Transform, part I: Resolution of the Wavefront Set*, Applied Computational Harmonic Analysis, Vol. 19, pp. 162–197, 2003.
- [10] E.J. CANDÈS AND D.L. DONOHO, *Continuous Curvelet Transform, part II: Discretization and Frames*, Applied Computational Harmonic Analysis, Vol. 19, pp. 198–222, 2003.
- [11] E.J. CANDÈS AND L. DEMANET AND D.L. DONOHO AND L. YING, *Fast discrete curvelet transforms*, SIAM Multiscale Modeling and Simulation, Vol. 5, pp. 861–899, 2005.
- [12] CHRISTOPHE DAMERVAL AND SYLVAIN MEIGNEN AND VALÉRIE PERRIER, *A Fast Algorithm for Bidimensional EMD*, IEEE Signal Processing Letters, Vol. 12, No. 10, pp. 701–704, 2005.
- [13] I. DAUBECHIES, *Ten Lectures on Wavelets*, Society for Industrial and Applied Mathematics, Cbms-Nsf Regional Conference Series in Applied Mathematics, 1992.
- [14] J. DELON AND A. DESOLNEUX AND J.L. LISANI AND A.B. PETRO, *A Nonparametric Approach for Histogram Segmentation*, IEEE Transactions on Image Processing, Vol. 16, No. 1, pp. 253–261, 2007.

- [15] A. DESOLNEUX AND L. MOISAN AND J-M. MOREL, *From Gestalt Theory to Image Analysis: A Probabilistic Approach*, Springer-Verlag, Interdisciplinary Applied Mathematics, Vol. 34, 2008.
- [16] D.L. DONOHO, *Ridge Functions and Orthonormal Ridgelets*, Journal of Approximation Theory, Vol. 111, pp. 143–179, 1998.
- [17] J. GILLES, *Empirical wavelet transform*, IEEE Transactions in Signal Processing, Vol. 61, No. 16, pp. 3999–4010, 2013.
- [18] L. GRAFAKOS AND W. ARBER, *Classical Fourier analysis*, Springer-Verlag New York, Current Topics in Microbiology and Immunology, Second Edition, 2008.
- [19] N.E. HUANG AND Z. SHEN AND S.R. LONG AND M.C. WU AND H.H. SHIH AND Q. ZHENG AND N-C. YEN AND C.C. TUNG AND H.H. LIU, *The empirical mode decomposition and the Hilbert spectrum for nonlinear and non-stationary time series analysis*, Proceedings of the Royal Society London Academy, Vol. 454, pp. 903–995, 1998.
- [20] E. LE PENNEC AND S. MALLAT, *Bandelet Image Approximation and Compression*, SIAM Journal on Multiscale Modeling and Simulation, Vol. 4, No. 3, pp. 992–1039, 2005.
- [21] E. LE PENNEC AND S. MALLAT, *Sparse geometric image representations with bandelets*, IEEE Trans. Image Processing, Vol. 14, No. 4, pp. 423–438, 2005.
- [22] S. MALLAT, *Geometrical Grouplets*, Applied and Computational Harmonic Analysis, Vol. 26, No. 2, pp. 161–180, 2009.
- [23] F.G. MEYER AND R.R. COIFMAN, *Brushlets: A tool for directional image analysis and image compression*, Applied and Computational Harmonic Analysis, Vol. 4, pp. 147–187, 1997.
- [24] J.C. NUNES AND Y. BOUAOUNE AND E. DELÉCHELLE AND N. OUMAR AND P. BUNEL, *Image analysis by bidimensional empirical mode decomposition*, Image and Vision Computing Journal (IVC), Vol. 21, pp. 1019–1026, 2003.
- [25] G. PEYRÉ AND S. MALLAT, *Discrete bandelets with geometric orthogonal filters*, Proceedings of International Conference on Image Processing (ICIP), pp. 65–68, 2005.
- [26] J.P. SERRA, *Image analysis and mathematical morphology*, Image Analysis and Mathematical Morphology Series, Vol. 1, Academic Press, 1982.
- [27] Z. SHEN, *Wavelet frames and image restorations*, Proceedings of the International Congress of Mathematicians, Rajendra Bhatia eds, Vol. 4, pp. 2834–2863, 2010.
- [28] P. SOILLE, *Morphological Image Analysis*, Springer-Verlag, Berlin, 1999.

- [29] J.L. STARCK AND M. ELAD AND D.L. DONOHO, *Image Decomposition Via the Combination of Sparse Representation and a Variational Approach*, IEEE Transactions on Image Processing, Vol. 14, No. 10, pp. 1570–1582, 2005.
- [30] Z. WANG AND A.C. BOVIK AND H.R. SHEIKH AND E. P. SIMONCELLI, *Image quality assessment: From error visibility to structural similarity*, IEEE Transactions on Image Processing, Vol. 13, No. 4, pp. 600–612, 2004.